

Generative artificial intelligence in ophthalmology: multimodal retinal images for the diagnosis of Alzheimer’s disease with convolutional neural networks

Slootweg, I.R. Thach, M. Curro-Tafili, K.R. Verbraak, F.D. Bouwman, F.H. Pijnenburg, Y.A.L. Boer, J.F. de Kwisthout, J.H.P. Bagheriye, L. González, P.J.

June 27, 2024

arXiv:2406.18247v1 [eess.IV] 26 Jun 2024

1 Synopsis

Denosing diffusion probabilistic models can generate retinal images suitable for augmenting training datasets. Deep learning shows promise for non-invasive Amyloid Positron Emission Tomography status prediction, with best performance using multimodal retinal imaging and metadata.

2 Abstract

Background/Aim: This study aims to predict Amyloid Positron Emission Tomography (AmyloidPET) status with multimodal retinal imaging and convolutional neural networks (CNNs) and to improve the performance through pretraining with synthetic data.

Methods Fundus autofluorescence, optical coherence tomography (OCT), and OCT angiography images from 328 eyes of 59 AmyloidPET positive subjects and 108 AmyloidPET negative subjects were used for classification. Denosing Diffusion Probabilistic Models (DDPMs) were trained to generate synthetic images and unimodal CNNs were pretrained on synthetic data and finetuned on real data or trained solely on real data. Multimodal classifiers were developed to combine predictions of the four unimodal CNNs with patient metadata. Class activation maps of the unimodal classifiers provided insight into the network’s attention to inputs.

Results DDPMs generated diverse, realistic images without memorization. Pretraining unimodal CNNs with synthetic data improved AUPR at most from 0.350 to 0.579. Integration of metadata in multimodal CNNs improved AUPR from 0.486 to 0.634, which was the best overall best classifier. Class activation maps highlighted relevant retinal regions which correlated with AD.

Conclusion Our method for generating and leveraging synthetic data has the potential to improve AmyloidPET prediction from multimodal retinal imaging. A DDPM can generate realistic and unique multimodal synthetic retinal images. Our best-performing unimodal and multimodal classifiers were not pretrained on synthetic data, however pretraining with synthetic data slightly improved classification performance for two out of the four modalities.

What is already known on this topic Alzheimer’s disease (AD) is diagnosed through invasive and expensive methods such as Amyloid Positron Emission Tomography (AmyloidPET) and cerebrospinal fluid analysis. The retina shows potential for non-invasive AD diagnostics with convolutional neural networks through imaging techniques like optical coherence tomography (OCT), OCT angiography and Fundus Scanning Laser Ophthalmoscopy (CNNs) but this is limited by the availability of few and small datasets.

What this study adds This study demonstrates that synthetic multimodal retinal images generated by a DDPM are suitable for augmenting training datasets and pretraining CNNs on synthetic data can enhance the diagnostic accuracy for AmyloidPET.

How this study might affect research, practice, or policy The findings suggest that generative AI holds promise for improving non-invasive AmyloidPET diagnosis. In turn, this allows for community-based AD screening, and offers a cost-effective and accessible alternative to current methods.

3 Introduction

Alzheimer’s disease (AD) is a progressive neurodegenerative condition that starts years before symptoms appear and poses an important public healthcare concern due to aging populations worldwide.[1] The disease is currently irreversible. Therefore, AD drug research is focused on early treatment to delay or prevent the development into dementia.[2] Current clinical

diagnosis relies on detection of decreased amyloid-beta levels, increased total tau and phosphorylated tau levels in the cerebrospinal fluid as well as imaging amyloid protein deposition in the brain using an Amyloid Positron Emission Tomography (AmyloidPET).[3] These techniques, however, are expensive and invasive and not practical for community-based screening for early onset of AD.

The retina is derived from the same embryological tissue as the brain and easily accessible for non-invasive screening via widely available imaging techniques such as Optical Coherence Tomography (OCT), OCT Angiography (OCT-A) and Fundus Scanning Laser Ophthalmoscopy photography (FSLO). Studies have associated retinal imaging parameters with AD.[4–8] These studies revealed abnormalities in the retinal nerve fiber layer, blood vessels and the optic nerve that correlate with changes in the brain of patients with AD.

Advances in artificial intelligence (AI) have allowed for the development of parameter-based and image-based classification models for the prediction of AD. Most studies focus on brain MRI and rarely on retinal imaging-based classification.[9–11] In turn, inputs of most retinal imaging-based implementations rely on the selection and manual extraction of image-derived features which can introduce information loss. However, several studies tried to mitigate these problems by developing convolutional neural networks (CNNs) for AD-related predictions with multimodal retinal images. But adding retinal imaging (AUROC = 0.836) to an existing set of inputs encompassing ganglion cell-inner plexiform layer maps, quantitative data and patient data (AUROC = 0.841) from 284 eyes of 159 subjects, did not improve performance of AD detection.[12] In a follow-up paper, distinction between mild cognitive impairment and normal cognition based on only OCT-A images (AUROC = 0.625) underperformed classification on image-derived quantitative data (AUROC = 0.960). These results indicate that it can be difficult to extract meaningful features from retinal imaging, especially in a small dataset.

CNNs rely on large image datasets, which is not always available in the medical imaging domain. To overcome this, generative artificial intelligence (AI) could extend the training dataset by synthesizing image data. Several approaches to generative AI exist, among which Diffusion Probabilistic Models (DDPMs).[13] DDPMs have gained significant popularity in the field of medical imaging and demonstrate superior output diversity compared to as Generative Adversarial Networks and Variational Auto Encoders.[14] However, DDPMs are more prone to memorization.[15, 16] DDPMs generate synthetic images by iteratively removing noise from an initial image made of pure Gaussian noise.[17] Class-conditioning the DDPM allows one model to generate images with varying content, for example of a specific animal, or medical images of a specific disease.

This study aims to predict AmyloidPET status with multimodal retinal imaging and to improve the performance through pretraining with synthetic data. A DDPM was developed to generate synthetic images for four types of retinal scans and a filter was created to recognize realistic synthetic images. Lastly, a multimodal classifier was trained to fuse unimodal predictions and patient information. The design of this framework serves as proof of concept for leveraging generative AI in classification tasks in ophthalmology.

4 Materials and Methods

4.1 Participants

Data from 183 patients of two retrospective cohorts with ophthalmic examinations including FSLO, conventional OCT and OCT-A were used. 328 eyes of 167 subjects were used: 116 eyes of 59 AmyloidPET positive (AmyloidPET+) subjects and 212 eyes of 108 AmyloidPET negative (AmyloidPET-) subjects. 203 eyes were part of the PreclinAD cohort consisting of cognitively healthy participants (monozygotic twins) aged ≥ 60 . [18–21] The remaining 125 eyes were part of an ongoing trial of the Alzheimer Center Amsterdam (METC 2019.623) which included participants aged ≥ 50 years. See Appendix for further description of the cohorts.

4.2 Datasets

The dataset contained in total 30 different modalities extracted from FSLO, OCT and OCT-A examinations. Four modalities from three scanner types covering the macula, optic nerve head (ONH) and fundus were selected for image synthesis and as inputs to the classification networks: 1) 2D OCT-A of the superficial retinal layers of the macula (OCTA-SMAC); 2D OCT B-Scan (OCT-B) of the 2) ONH (OCT-BONH); and 3) macula (OCT-BMAC); and 4) 2D FSLO autofluorescence (FAF). Images in the datasets were included based on image quality and the modalities were selected after the development of generative models for a larger set of eight modalities, as described in the Appendix. We created overlapping collections for the development of: generative models (D_{synth}); a modality recognition classifier (D_{filter}); unimodal classifiers (D_{uni}); and multimodal classifiers (D_{multi}). Of the 328 eyes in this dataset, 198 eyes were included in D_{multi} , 326 in D_{uni} and 328 in D_{synth} and D_{filter} (Table 1).

Subset	[N] eyes (All)	[N] Images (All)	[N] eyes (Dev)	[N] images (Dev)	[%] AmyloidPET+ (Dev)	[N] eyes (Test)	[N] images (Test)	[%] AmyloidPET+ (Test)
Multimodal classification	198	198	160	160	0.394	38	38	0.368
Unimodal classification	326	1080	285	869		83	211	
- OCTA-SMAC	276	276	223	223	0.400	53	53	0.396
- OCT-BONH	278	278	220	220	0.429	58	58	0.379
- OCT-BMAC	276	276	220	220	0.426	56	56	0.411
- FAF	250	250	206	206	0.354	44	44	0.364
Synthesis	328	1102						
- OCTA-SMAC	276	276	223	223	0.386	53	53	0.396
- OCT-BONH	278	278	220	220	0.377	58	58	0.379
- OCT-BMAC	276	276	220	220	0.382	56	56	0.411
- FAF	254	272	210	225	0.351	44	47	0.340

Table 1: Datasets used for training and validation (development, Dev) and testing (Test). Images without known AmyloidPET status were excluded from the classification sets. The first split between testing, training and validation was created for D_{multi} with 198 eyes with known AmyloidPET status and available images for all four modalities. The remaining 128 eyes with images for at least one of the selected modalities and known AmyloidPET status were distributed over these splits to create the D_{uni} collection. This totals to 1080 images used for unimodal classification. 22 images with known AmyloidPET status from duplicate FAF recordings were added to these splits to create D_{synth} . The training, validation and test splits of the collections were created in this way to prevent information leakage between training and evaluation sets of the collections.

4.3 Models

The pipeline for data synthesis and for training the classification networks are depicted in Figure 1. Our approach involved the generation of a synthetic image dataset, development of a filter to ensure high-quality synthetic images, and training unimodal and multimodal classifiers to predict AmyloidPET status. See Appendix for details of the network architectures and hyperparameters governing the training trajectories.

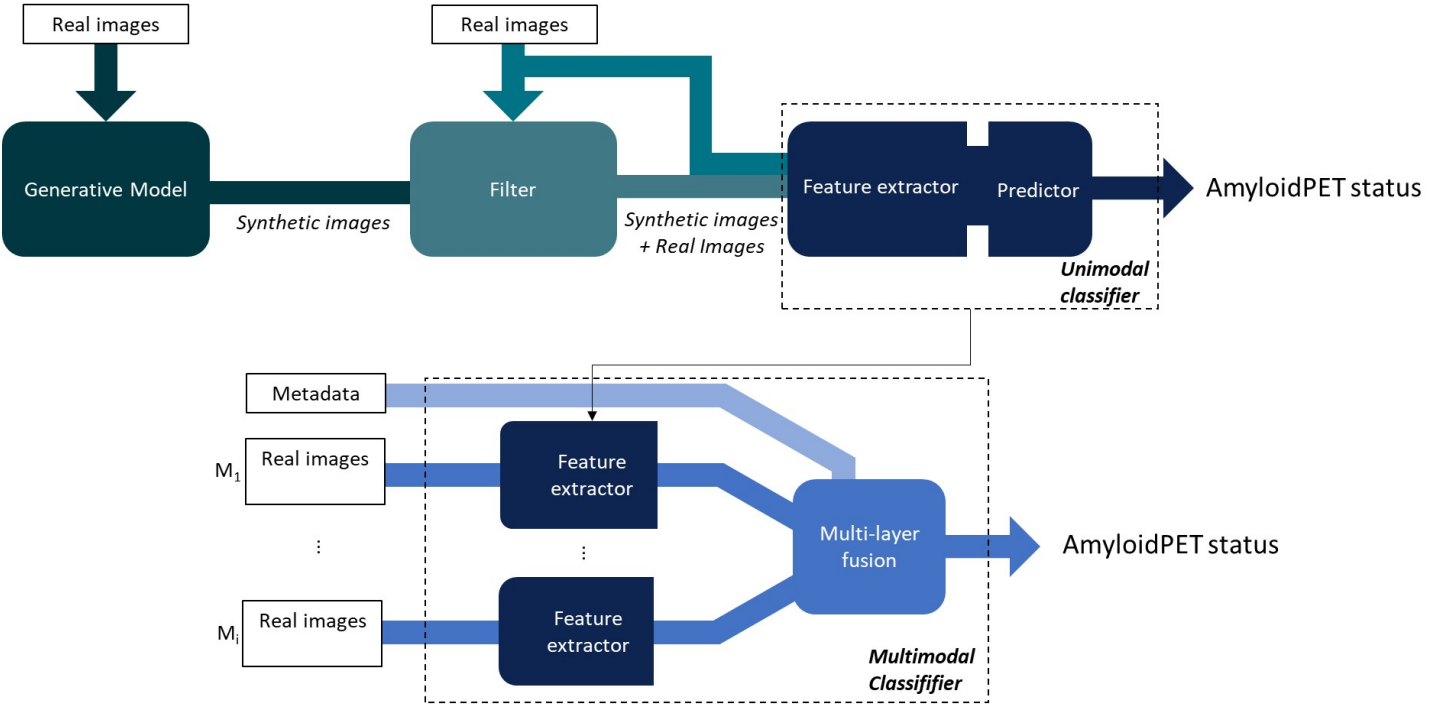


Figure 1: Illustration of the pipeline. (Top): Synthetic images were generated by a DDPM. The synthetic images for which the filter could recognize the modality were included in the training budget of 1000 synthetic images per class. Both synthetic and real images were used to train unimodal classifiers for predicting AmyloidPET status. We created 'baseline' unimodal classifiers trained on real images, and 'pretrained' unimodal classifiers pretrained on 1000 synthetic images per class and finetuned on real images. Unimodal classifiers were not trained with metadata inputs because synthetic data, which has no associated age and gender, was used for pretraining. (Bottom): We compared multimodal classifiers with the baseline and pretrained unimodal classifiers. The weights of unimodal classifiers were fixed after training. A three-layer fully connected network (FC) performed late heterogeneous fusion of the unimodal predictions and metadata into one AmyloidPET probability prediction. If metadata was included as inputs, age (binary) and gender (scaled by 0.01) metadata were also fed to the FC. Output of the unimodal and multimodal classifiers were scored between 0 and 1 for the probability of AmyloidPET negative status.

4.3.1 Synthetic images

We used a conditional U-Net DDPM for generating synthetic images corresponding to specific AmyloidPET status. The DDPM model was selected based on the quality of the synthetic images and the required training time. A potential for memorization of the training images exists in a dataset with DDPMs. Therefore, we evaluated the diversity and uniqueness of generated images using a random sample of 200 synthetic images and all real images.[15] The maximum Pearson’s correlation coefficient (pearsonr) of one image from an arbitrary set A with all images in a different set B expresses how similar this image is at most to set B . In the case of memorization the distribution of maximum correlation values of all synthetic images with the set of real images would be high. The diversity of synthetic images was evaluated by comparing the distribution of maximum pearsonr values among real images and among synthetic images. With Wasserstein Distance (WD) we expressed the difference between two distributions of correlation values, Kolmogorov–Smirnov (KS) test informed the significance of such differences.

4.3.2 Filter

We assumed that for generated images with large artifacts or deformations, it would be more difficult to recognize the modality type. Therefore, a CNN was trained to recognize the modality of images and then applied to detect unrealistic synthetic images. Images with incorrectly recognized modalities were discarded. The filter was evaluated with Matthew’s Correlation Coefficient (MCC) for a balanced evaluation of the filter’s overall performance by correlating the outputs, between 0 and 1 for each class, and the ground truth labels.[22]

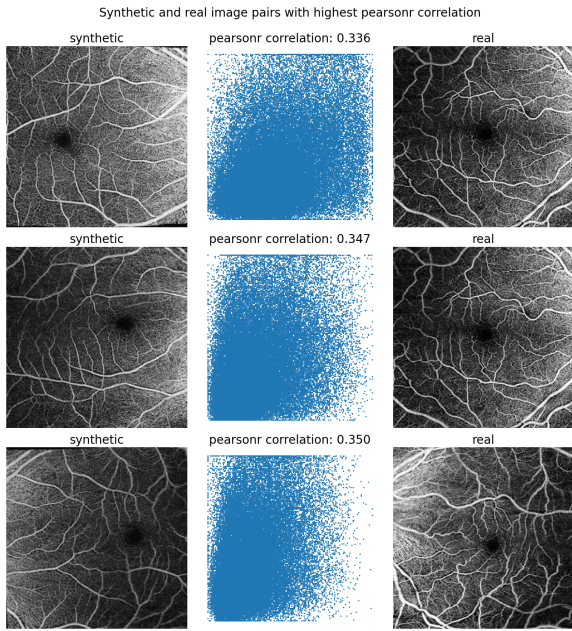
4.3.3 Classification

Unimodal classifiers were developed for all modalities to predict AmyloidPET status. The EfficientNet-B0 backbone without pretrained ImageNet weights showed best loss reduction in small (25 trials) hyperparameter optimization experiments.[23] Unimodal classifiers were pretrained with synthetic images and subsequently finetuned on real data. The FC of multimodal classifiers was trained with outputs of the unimodal classifiers, per eye, and metadata. Performance was evaluated on the validation and test sets, reported by area under the receiver operator curve (AUROC), area under the precision recall curve (AUPR), sensitivity, specificity and F1-score as harmonic mean between sensitivity and precision. With class activation maps (CAMs) we attempted to gain insights into the CNN predictions. CAMs indicated which discriminative image regions contributed to a model’s output value.[24] As our model outputted the probability for AmyloidPET-, the resulting heatmap displayed the image regions that contributed to an output of a higher probability of AmyloidPET-.

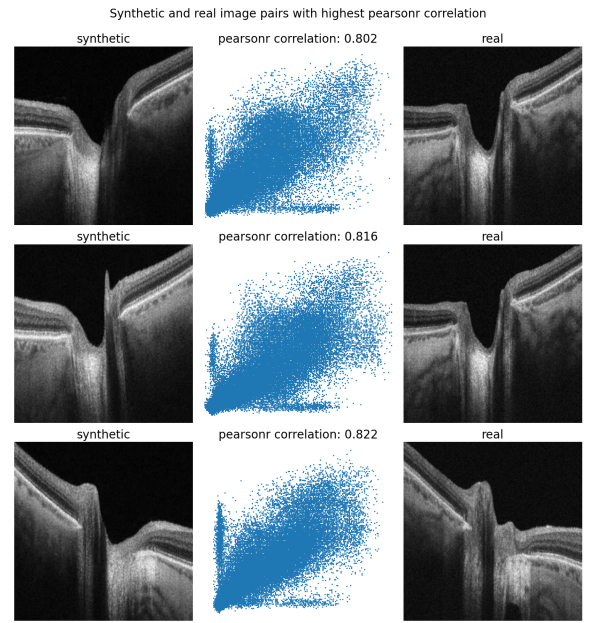
5 Results

5.1 Synthetic data

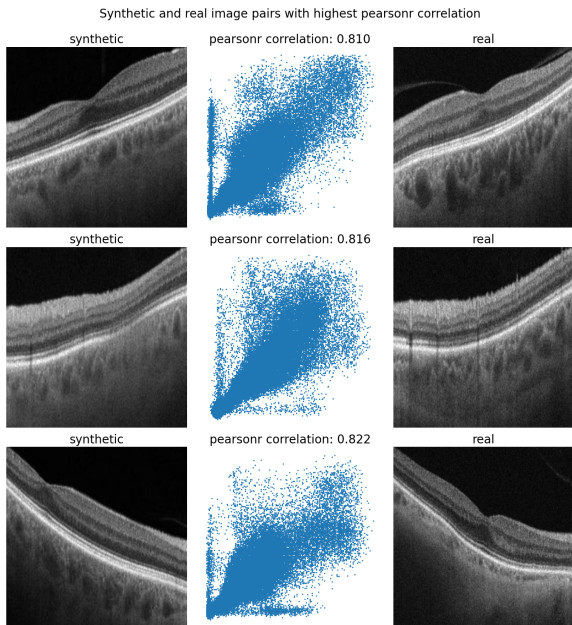
Examples of synthetic images are shown in Figure S1 in the Appendix. Figure 2 displays, for each modality, the three synthetic images with the highest correlation with any real image and the corresponding real image. Visual inspection of these examples illustrates that it depended on the nature of a modality whether pearsonr of the pixel values was in good agreement with the visual similarity of retinal images. Figure 3 displays distributions of the maximum correlation for synthetic images with all real images (SvR), among the real images (RvR), and among synthetic images (SvS). We observed little memorization in the generated data as the SvR distributions did not reach close to 1. However, we discovered a positive trend between SvR and RvR values (pearsonr =0.997): if for a modality the similarity amongst real images was high, the similarity between real images and synthetic images was also high. This could be caused by characteristics of the modalities (Figure 2). We compared SvR with RvR for each modality to provide extra context on the extend of memorization. Similarity of synthetic images to real images did not exceed the similarity among real images for any of the modalities, which weakens the concern for memorization. SvS was stronger than RvR for OCTA-SMAC (WD = 0.025, p=1.22e⁻⁶) and FAF (WD = 0.027, p=8.079e⁻¹¹), implying reduced diversity of the synthetic images of these modalities. However, the distribution plots in Figure 3 display that these differences between between the RvR and SvS distributions are minimal.



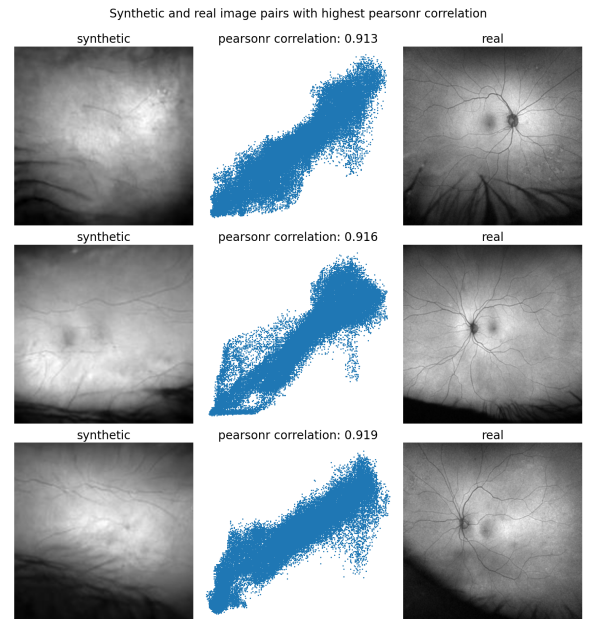
(a)



(b)



(c)



(d)

Figure 2: Examples of the synthetic images with the highest correlation to any real image. Pairs of synthetic images and the corresponding real image that it most closely resembles are displayed together with scatter plot of the pixel values and the correlation value. (a) OCTA-SMAC; (b) OCT-BONH; (c) OCT-BMAC; (d) FAF. For OCT-BMAC and OCT-BONH the synthetic images strongly resembled the real images but were not exact copies. For OCTA-SMAC and FAF the images with the highest correlations showed less resemblance. This was also reflected by the lower correlation values for OCTA-SMAC. FAF exhibited the highest distribution of maximum correlation values. These images consisted of a predominantly grey background which contributed to a high correlation between any two images of this modality.

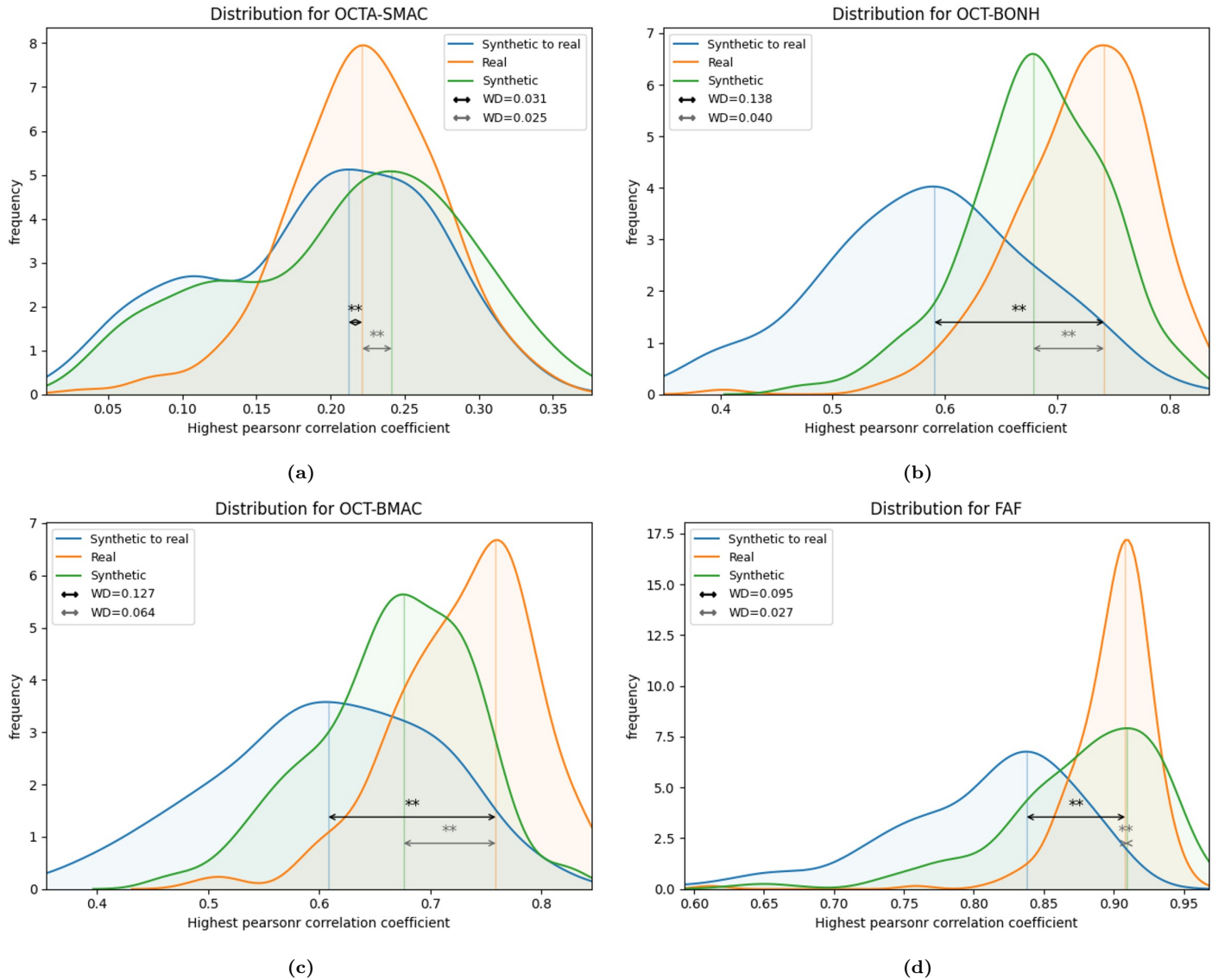


Figure 3: (A-D): Distributions for maximum pearsonr values computed for 200 synthetic images and all real images. Distributions display the highest correlation for image pairs among real images (RvR, orange), among synthetic images (SvS, green) and for all synthetic images with any real image (SvR, blue). Arrows indicate the differences between SvR and RvR distributions (black) and the differences between RvR and SvS distributions (grey). WD values express the distance between two distributions with KS test p-values for the significance of such differences. pearsonr = Pearson’s correlation coefficient. ** = $p < 0.005$

5.2 Filter

The trained filter model achieved 99% accuracy for recognizing the modalities on the test set with MCC of 0.990 for the predictions on the validation set and MCC of 0.997 on the test set (Table S1). The model performed so well that it could correctly recognize the modality of unrealistic synthetic images of type OCTA-SMAC, OCT-SONH and OCT-SMAC, diminishing its role in detecting unrealistic images. Therefore, we applied a manually set threshold on the model outputs for these three modalities; 0.90, 0.99 and 0.96, respectively. Any sampled synthetic image was included in our synthetic dataset if the predicted modality was correct and if the confidence for this modality satisfied this threshold.

5.3 Classification

Table 2 displays the results of classification experiments. Pretraining on synthetic data showed slight AUPR improvement for OCT-BONH, OCT-BMAC and FAF on the validation set, as well as for OCTA-SMAC and OCT-BMAC on the test set. The overall best model on the test set was the multimodal classifier trained on real data (AUPR 0.634, F1-score 0.625). The best unimodal classifier in terms of AUPR was OCTA-SMAC trained on synthetic data (AUPR 0.613). In terms of F1-score, the pretrained OCT-BMAC classifier performed best (F1-score 0.596). In several models, finetuning on real data showed a reduction of performance compared to the models trained on synthetic data.

	AUPR			AUROC			F1-score			Sensitivity			Specificity		
	Real	Synth.	Pretr.	Real	Synth.	Pretr.	Real	Synth.	Pretr.	Real	Synth.	Pretr.	Real	Synth.	Pretr.
Validation															
Unimodal															
- OCTA-SMAC	0.583	0.632	0.436	0.646	0.690	0.583	0.635	0.695	0.565	0.909	0.740	0.591	0.364	0.610	0.667
- OCT-BONH	0.573	0.593	0.617	0.602	0.617	0.707	0.553	0.560	0.690	0.542	0.510	0.833	0.688	0.690	0.563
- OCT-BMAC	0.611	0.569	0.665	0.668	0.577	0.728	0.655	0.605	0.667	0.826	0.650	0.739	0.484	0.500	0.645
- FAF	0.545	0.864	0.576	0.744	0.858	0.664	0.629	0.811	0.519	0.647	0.835	0.412	0.774	0.775	0.903
Multimodal															
- No metadata	0.406	-	0.632	0.567	-	0.708	0.600	-	0.571	0.800	-	0.533	0.458	-	0.792
- With metadata	0.456	-	0.467	0.631	-	0.592	0.588	-	0.636	0.667	-	0.933	0.625	-	0.375
Test															
Unimodal															
- OCTA-SMAC	0.338	0.613	0.455	0.381	0.647	0.586	0.381	0.541	0.522	0.381	0.476	0.571	0.594	0.813	0.594
- OCT-BONH	0.488	0.368	0.481	0.530	0.412	0.583	0.533	0.545	0.489	0.727	0.955	0.500	0.389	0.056	0.667
- OCT-BMAC	0.350	0.451	0.579	0.391	0.569	0.615	0.426	0.571	0.596	0.435	0.696	0.739	0.576	0.485	0.485
- FAF	0.390	0.310	0.347	0.549	0.326	0.478	0.571	0.100	0.489	0.875	0.063	0.688	0.321	0.893	0.357
Multimodal															
- No metadata	0.486	-	0.441	0.622	-	0.491	0.500	-	0.333	0.500	-	0.286	0.708	-	0.750
- With metadata	0.634	-	0.306	0.729	-	0.369	0.625	-	0.531	0.714	-	0.929	0.667	-	0.083

Table 2: Classification results for the validation set and test set. Real = trained on real data. Synth. = trained on synthetic data. Pretr = pretrained on synthetic data and finetuned on real data. Precision and recall were determined based on a threshold obtained with the youden’s index.

5.4 Class activation maps

Figures S5-S7 display test images with GradCAMs that identified the regions of the image that contributed to a higher model output. We compared the GradCAMs in Figure S5 and S6 to interpret and compare the outputs of the baseline and pretrained classifiers. We also reviewed the GradCAMs of the classifier trained on synthetic images (Figure S7) to discover whether a model trained on synthetic data could identify relevant areas in the images. We observed different responses to real images by the various classifiers. For example, in OCTA-SMAC, attention of the baseline classifier to blood vessels in the periphery switched to the center of the image by the pretrained classifier. The baseline OCT-BONH classifier showed high response to small areas in the layers of the retina. The shape and location of the attention in the OCT-BONH models implied that meaningful features were learned, however the output values for the different classes were very close to each other (0.494 and 0.485 compared to 0.471 and 0.489) which implied that the classes were not well distinguished by these features. The pretrained FAF classifier identified areas around the fovea and ONH.

6 Discussion

To our knowledge, this is the first study to generate multimodal synthetic image data to detect AmyloidPET status using retinal imaging. Akbar et al.[15] noted that diffusion models are prone to memorizing training images, especially with small datasets. However, we were able to construct a DDPM that was capable of generating synthetic retinal images with our small dataset. The synthetic images were unique and not copies of the limited number of real images we provided. Furthermore, we hypothesized that these synthetic images contained relevant information for predicting AmyloidPET status on real images. A small dataset can lead to a classifier’s inability to recognize salient image features due to overfitting on the training data. To mitigate this, we supplemented the development set with 1000 images per AmyloidPET class, generated by a conditional DDPM. Pretraining CNNs with synthetic data slightly improved classification performance for two out of four modalities in terms of AUPR and improved F1-score for one modality. This suggests that exploiting synthetic data can enhance CNN performance in small datasets for medical image classification. Further research into synthetic data training budgets, synthesis methods, and exploitation strategies could demonstrate the potential of generative AI for deep learning in medical imaging.

Our best unimodal and multimodal classifiers were not pretrained on synthetic data. Finetuning on real data sometimes reduced performance of unimodal classifiers, possibly due to low similarity of the real and synthetic images of these modalities. Our best model used multimodal FSLO, OCT, and OCT-A inputs and metadata, and achieved AUPR of 0.634 (AUROC 0.729) on the test set, outperforming our best unimodal classifiers. By including metadata, the performance of the multimodal classifier improved from AUPR 0.486 (AUROC 0.622). Wisely et al.[12] and Cheung et al.[25] observed similar improvements, for AD and AmyloidPET prediction respectively, although the differences were not significant. It should be noted that AmyloidPET detection differs from AD diagnosis as cognitively healthy individuals can have a positive AmyloidPET scan. Additionally, it may be worthwhile to investigate the effect of unilateral and bilateral inputs for our models as Cheung et al.[25] found that bilateral inputs improved AmyloidPET status prediction compared to unilateral inputs (AUROC = 0.68 - 0.86 vs. 0.61 - 0.83 on external validation). However, it must be noted that we would have limited training samples for the bilateral predictions due to our dataset size.

In our study, FAF-based models performed poorly compared to other classifiers, aligning with the results of Wisely et al.[12], as they concluded that FSLO images have low utility for predicting AD diagnosis. Our suggestion for future experiments is

to explore metadata incorporation into unimodal classifiers, which requires adaptation for pretraining without metadata and subsequent finetuning with metadata. However, incorporating metadata can have mixed effects. Cheung et al.[25] argue that not requiring patient data is advantageous. Although excluding patient information such as age and gender could prevent CNNs from biasing towards patient groups of certain demographics, learning from patient age and gender may actually be valuable as these characteristics can affect retinal structure, aiding feature extraction and prediction.[26, 27] The superior performance with metadata observed by Wisely et al.[12] as well as our study may be due to the inclusion of additional OCT-derived modalities alongside FSLO, which provide higher axial resolution. This diversity of inputs can offer more opportunity for utilization of metadata in processing unimodal predictions.

As the first study to use synthetic retinal images for AmyloidPET prediction, we evaluated the models' internal states with heatmaps to visualize learned knowledge. GradCAM heatmaps in Figures S7 indicate that training on synthetic images can teach a model to recognize salient regions in real images. Specifically, a CNN based on OCTA-SMAC pretrained on synthetic images and finetuned on real images draws attention towards the center of the images, which is where the foveal avascular zone is located, an area associated with AD in several meta-analyses.[7, 28] Existing studies have provided saliency maps for fundus-based AD prediction and showed that small blood vessels and the main vascular branches are most salient.[25, 29] Our FAF classifier trained on real images projected similar attention on synthetic images, highlighting main vascular branches, with the synthetic-trained classifier showing similar attention on small vascular branches in real images.

Limitations of this study are related to the nature of the training and validation sets. It is difficult to fit models that generalize well on unseen data because of our small dataset. Furthermore, performance on the evaluation dataset may not be good indicators of the performance of our methods, as the composition of the evaluation dataset influences the performance and may greatly vary depending on the split. We used stratified splits to address this but additional cross-validation experiments would yield more reliable results. A larger dataset could also mitigate these issues.

References

1. Rasmussen J and Langerman H. Alzheimer's Disease – Why We Need Early Diagnosis. *Degenerative Neurological and Neuromuscular Disease* 2019 Dec; Volume 9:123–30. DOI: 10.2147/dnnd.s228939
2. Wu W, Ji Y, Wang Z, Wu X, Li J, Gu F, Chen Z, and Wang Z. The FDA-approved anti-amyloid- β monoclonal antibodies for the treatment of Alzheimer's disease: a systematic review and meta-analysis of randomized controlled trials. *Eur. J. Med. Res.* 2023 Nov; 28:544
3. McKhann GM, Knopman DS, Chertkow H, Hyman BT, Jack CR, Kawas CH, Klunk WE, Koroshetz WJ, Manly JJ, Mayeux R, Mohs RC, Morris JC, Rossor MN, Scheltens P, Carrillo MC, Thies B, Weintraub S, and Phelps CH. The diagnosis of dementia due to Alzheimer's disease: Recommendations from the National Institute on Aging-Alzheimer's Association workgroups on diagnostic guidelines for Alzheimer's disease. *Alzheimer's & Dementia* 2011 Apr; 7:263–9. DOI: 10.1016/j.jalz.2011.03.005
4. Zhang J, Shi L, and Shen Y. The retina: A window in which to view the pathogenesis of Alzheimer's disease. *Ageing Research Reviews* 2022 May; 77:101590. DOI: 10.1016/j.arr.2022.101590
5. Cheung CY, Mok V, Foster PJ, Trucco E, Chen C, and Wong TY. Retinal imaging in Alzheimer's disease. *Journal of Neurology, Neurosurgery & Psychiatry* 2021 Jun; 92:983–94. DOI: 10.1136/jnnp-2020-325347
6. Zabel P, Kaluzny JJ, Zabel K, Kaluzna M, Lamkowski A, Jaworski D, Makowski J, Gebaska-Toloczek M, and Kucharski R. Quantitative assessment of retinal thickness and vessel density using optical coherence tomography angiography in patients with Alzheimer's disease and glaucoma. *PLOS ONE* 2021 Mar; 16. Ed. by Lewin AS:e0248284. DOI: 10.1371/journal.pone.0248284
7. Jin Q, Lei Y, Wang R, Wu H, Ji K, and Ling L. A Systematic Review and Meta-Analysis of Retinal Microvascular Features in Alzheimer's Disease. *Frontiers in Aging Neuroscience* 2021 Jun; 13. DOI: 10.3389/fnagi.2021.683824
8. Salazar J, Ramirez A, Hoz R de, and Rojas P. Amyotrophic lateral sclerosis, a neurodegenerative motor neuron disease with retinal involvement. *Neural Regeneration Research* 2022; 17:1011. DOI: 10.4103/1673-5374.324841
9. Basaia S, Agosta F, Wagner L, Canu E, Magnani G, Santangelo R, and Filippi M. Automated classification of Alzheimer's disease and mild cognitive impairment using a single MRI and deep neural networks. *NeuroImage: Clinical* 2019; 21:101645. DOI: 10.1016/j.nicl.2018.101645
10. Amoroso N, Diacono D, Fanizzi A, La Rocca M, Monaco A, Lombardi A, Guaragnella C, Bellotti R, and Tangaro S. Deep learning reveals Alzheimer's disease onset in MCI subjects: Results from an international challenge. *Journal of Neuroscience Methods* 2018 May; 302:3–9. DOI: 10.1016/j.jneumeth.2017.12.011
11. Wang X, Jiao B, Liu H, Wang Y, Hao X, Zhu Y, Xu B, Xu H, Zhang S, Jia X, Xu Q, Liao X, Zhou Y, Jiang H, Wang J, Guo J, Yan X, Tang B, Zhao R, and Shen L. Machine learning based on Optical Coherence Tomography images as a diagnostic tool for Alzheimer's disease. *CNS Neuroscience & Therapeutics* 2022 Sep; 28:2206–17. DOI: 10.1111/cns.13963
12. Wisely CE, Wang D, Henao R, Grewal DS, Thompson AC, Robbins CB, Yoon SP, Soundararajan S, Polascik BW, Burke JR, Liu A, Carin L, and Fekrat S. Convolutional neural network to identify symptomatic Alzheimer's disease using multimodal retinal imaging. *British Journal of Ophthalmology* 2020 Nov; 106:388–95. DOI: 10.1136/bjophthalmol-2020-317659
13. Ho J, Jain A, and Abbeel P. Denoising Diffusion Probabilistic Models. 2020. DOI: 10.48550/ARXIV.2006.11239
14. Kazerouni A, Aghdam EK, Heidari M, Azad R, Fayyaz M, Hacıhaliloğlu I, and Merhof D. Diffusion models in medical imaging: A comprehensive survey. *Medical Image Analysis* 2023 May :102846. DOI: 10.1016/j.media.2023.102846
15. Akbar MU, Wang W, and Eklund A. Beware of diffusion models for synthesizing medical images – A comparison with GANs in terms of memorizing brain MRI and chest x-ray images. 2023. DOI: 10.48550/ARXIV.2305.07644
16. Dhariwal P and Nichol A. Diffusion Models Beat GANs on Image Synthesis. 2021. DOI: 10.48550/ARXIV.2105.05233
17. Yang L, Zhang Z, Song Y, Hong S, Xu R, Zhao Y, Zhang W, Cui B, and Yang MH. Diffusion Models: A Comprehensive Survey of Methods and Applications. 2022. DOI: 10.48550/ARXIV.2209.00796
18. Boomsma DI, Geus EJCd, Vink JM, Stubbe JH, Distel MA, Hottenga JJ, Posthuma D, Beijsterveldt TCEMv, Hudziak JJ, Bartels M, and Willemsen G. Netherlands Twin Register: From Twins to Twin Families. *Twin Research and Human Genetics* 2006 Dec; 9:849–57. DOI: 10.1375/twin.9.6.849
19. Konijnenberg E, Carter SF, Kate M ten, Braber A den, Tomassen J, Amadi C, Wesselman L, Nguyen HT, Kreeke JA van de, Yaqub M, Demuru M, Mulder SD, Hillebrand A, Bouwman FH, Teunissen CE, Serné EH, Moll AC, Verbraak FD, Hinz R, Pendleton N, Lammertsma AA, Berckel BNM van, Barkhof F, Boomsma DI, Scheltens P, Herholz K, and Visser PJ. The EMIF-AD PreclinAD study: study design and baseline cohort overview. *Alzheimer's Research & Therapy* 2018 Aug; 10. DOI: 10.1186/s13195-018-0406-7

20. Kate M ten, Sudre CH, Braber A den, Konijnenberg E, Nivard MG, Cardoso MJ, Scheltens P, Ourselin S, Boomsma DI, Barkhof F, and Visser PJ. White matter hyperintensities and vascular risk factors in monozygotic twins. *Neurobiology of Aging* 2018 Jun; 66:40–8. DOI: 10.1016/j.neurobiolaging.2018.02.002
21. Kreeke JA van de, Nguyen HT, Konijnenberg E, Tomassen J, Braber A den, Kate M ten, Sudre CH, Barkhof F, Boomsma DI, Tan HS, Verbraak FD, and Visser PJ. Retinal and Cerebral Microvasculopathy: Relationships and Their Genetic Contributions. *Investigative Ophthalmology & Visual Science* 2018 Oct; 59:5025. DOI: 10.1167/iovs.18-25341
22. Chicco D and Jurman G. The advantages of the Matthews correlation coefficient (MCC) over F1 score and accuracy in binary classification evaluation. *BMC Genomics* 2020 Jan; 21. DOI: 10.1186/s12864-019-6413-7
23. Tan M and Le QV. EfficientNet: Rethinking Model Scaling for Convolutional Neural Networks. 2019. DOI: 10.48550/ARXIV.1905.11946
24. Selvaraju RR, Cogswell M, Das A, Vedantam R, Parikh D, and Batra D. Grad-CAM: Visual Explanations from Deep Networks via Gradient-Based Localization. *International Journal of Computer Vision* 2019 Oct; 128:336–59. DOI: 10.1007/s11263-019-01228-7
25. Cheung CY, Ran AR, Wang S, Chan VTT, Sham K, Hilal S, Venketasubramanian N, Cheng CY, Sabanayagam C, Tham YC, Schmetterer L, McKay GJ, Williams MA, Wong A, Au LWC, Lu Z, Yam JC, Tham CC, Chen JJ, Dumitrascu OM, Heng PA, Kwok TCY, Mok VCT, Milea D, Chen CLH, and Wong TY. A deep learning model for detection of Alzheimer’s disease based on retinal photographs: a retrospective, multicentre case-control study. *The Lancet Digital Health* 2022 Nov; 4:e806–e815. DOI: 10.1016/s2589-7500(22)00169-8
26. Polascik BW, Thompson AC, Yoon SP, Powers JH, Burke JR, Grewal DS, and Fekrat S. Association of OCT Angiography Parameters With Age in Cognitively Healthy Older Adults. *Ophthalmic Surgery, Lasers and Imaging Retina* 2020 Dec; 51:706–14. DOI: 10.3928/23258160-20201202-05
27. Munk MR, Kurmann T, Márquez-Neila P, Zinkernagel MS, Wolf S, and Sznitman R. Assessment of patient specific information in the wild on fundus photography and optical coherence tomography. *Scientific Reports* 2021 Apr; 11. DOI: 10.1038/s41598-021-86577-5
28. Ashraf G, McGuinness M, Khan MA, Obtinalla C, Hadoux X, and Wijngaarden P van. Retinal imaging biomarkers of Alzheimer’s disease: A systematic review and meta-analysis of studies using brain amyloid beta status for case definition. *Alzheimer’s & Dementia: Diagnosis, Assessment & Disease Monitoring* 2023 Apr; 15. DOI: 10.1002/dad2.12421
29. Tian J, Smith G, Guo H, Liu B, Pan Z, Wang Z, Xiong S, and Fang R. Modular machine learning for Alzheimer’s disease classification from retinal vasculature. *en. Sci. Rep.* 2021 Jan; 11:238

Appendix

Cohorts

203 eyes are part of the PreclinAD cohort which is an extension of the Amsterdam sub-study of the European Medical Information Framework for AD from the Amsterdam UMC, location VUmc.[1, 2] The PreclinAD cohort consists of cognitively healthy participants (monozygotic twins) from the Netherlands Twin Register who all underwent ophthalmic evaluation. The remaining 125 eyes are part of an ongoing trial of the Amsterdam Alzheimer Center (METC 2019.623). Both studies followed the Tenets of the Declaration of Helsinki and the Medical Ethics Committee of the VU University Medical Center in Amsterdam approved the studies. All participants signed an informed consent and underwent a screening protocol that included in short: ophthalmological examinations, (medical) history check-up, Mini Mental State Examination test and neuropsychological evaluations. Subjects with ischemic stroke, neurodegenerative disorders or systemic chronic conditions (i.e. Parkinson’s disease, Diabetes Mellitus and multiple sclerosis) were excluded.

Dataset

All scans were evaluated for image quality and availability of AmyloidPET status. Image quality for FSLO exams was reviewed based on movement or optical distortions such as lash or eyelid coverage and a straight eye gaze was required. OCT-A images were evaluated by focus and resolution and 3D OCT scans were evaluated on the same criteria.

The full image dataset covered retinal scans from three types of retinal modalities: Fundus SLO (Optos), OCT-A (Zeiss Angioplex) and volumetric OCT (Heidelberg OCT). The initial dataset included a set of 26 modalities. Optos: FAF and red-green fundus (FRG); Zeiss Angioplex: depth-encoded, and five layer-specific OCT-A and structural B-scan images for both the ONH and macula; Heidelberg: 3D volumetric cubes of the optic nerve and macula. Initial experiments were performed to create synthetic images for FAF, FRG, depth-encoded macula angiography (OCTA-EMAC), depth-encoded ONH angiography (OCTA-EONH), layer-specific OCT-A of the deep and superficial layers of the ONH (OCTA-DONH, OCTA-SONH) and macula (OCTA-DMAC, OCTA-SMAC). We also experimented with 3D DDPM for volumetric scans of the ONH (OCT-VONH) and macula (OCT-VMAC). The experiments failed to create realistic volumetric, depth-encoded and FRG images. Therefore, we made a selection of four modalities extracted from FSLO, OCT-A and structural OCT scans to maintain the variety of the inputs to the classification models. For FSLO we selected the FAF modality as we could not create realistic synthetic images for FRG. For OCT-A we used the superficial layer of the macula instead of the depth-encoded OCTA-EONH and OCTA-EMAC as most research suggests that changes in foveal avascular zone and vessel density in superficial macula may correlate with AD progression.[3–5] Instead of volumetric structural OCT we used 2D structural OCT-BONH and OCT-BMAC that were generated during the angiography recordings on the Zeiss Angioplex. A comparison of the 2D real and synthetic images for the initial and final DDPMs is depicted in Supplementary Figure S1.

Data splits

The first split between testing, training and validation was created for D_{multi} with eyes with known AmyloidPET status and available images for all selected modalities. The remaining eyes with images of at least one of the selected modalities and known AmyloidPET status were distributed over these splits to create the D_{uni} collection. Images with known AmyloidPET status from duplicate FAF recordings were added to these splits to create D_{synth} . Finally, the splits in D_{synth} were supplemented with images of modalities not selected for classification as well as images of eyes with unknown AmyloidPET status to form D_{filter} . The number of eyes in test splits was not expanded after D_{uni} was formed, meaning that supplementary eyes were added to the training and validation splits of D_{synth} and D_{filter} . We aimed to keep the proportion of AmyloidPET positives (AmyloidPET+) balanced while assigning 20% of the eyes to the test set and using 20% of the eyes in a collection for validation. Splits for these sets were performed at a family level to prevent information leakage as we dealt with monozygotic twin pairs in our dataset, whose retinal images may hold strong resemblance. For training the filter, images of 26 2D modalities were used, excluding 3D OCT of the macula and ONH for the volumetric nature of the data and excluding widefield FSLO recordings for the small dataset size of 74 autofluorescence and 76 red-green images. Furthermore, images without known AmyloidPET status were included for training the filter. Some eyes had duplicate FAF images with good image quality. In this case, one image per eye per modality was selected for classifier development. Duplicate images could be used for filter development and generative model development.

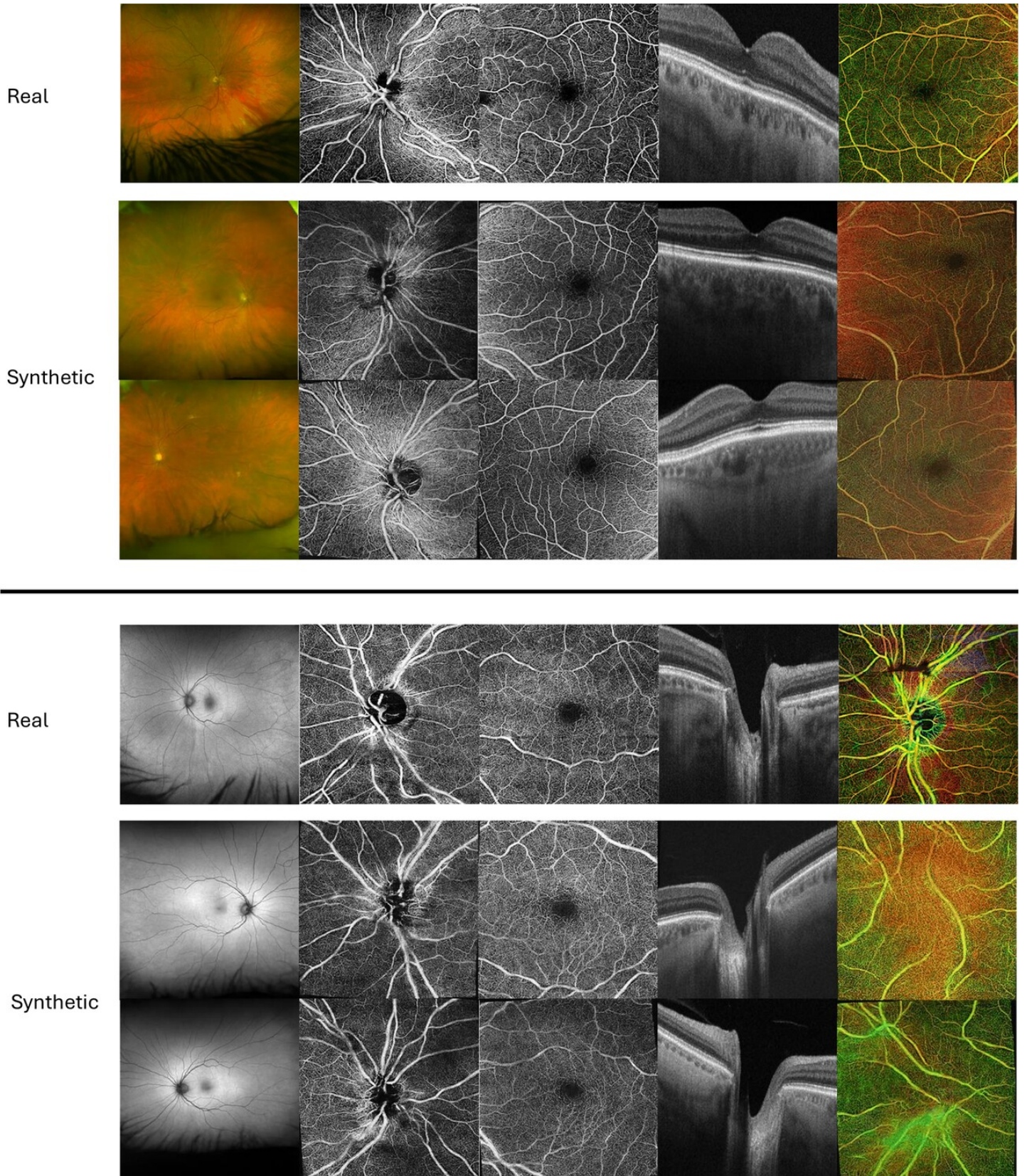


Figure S1: Examples of generated synthetic images and real images for eight modalities. Top row from left to right: FRG, OCTA-SONH, OCTA-SMAC; OCT-BMAC; OCTA-EMAC. Bottom row left to right: FAF; OCTA-DONH; OCTA-DMAC; OCT-BONH; OCTA-EONH. The synthetic FAF images best resembled their real counterpart, with often accurate branching of the bloodvessels and even replication of the eye lashes at the periphery of the image. Synthetic FRG images failed to replicate the vasculature. Furthermore, the images were not sharp and most of them lacked accurate colors and would be green or yellow similar to the depth-encoded images. Most of the OCT-A images failed to replicate accurate branching of the blood vessels. OCT B-Scan images were overall quite realistic, although sometimes replication of one or two layers in the retina would occur. Depth-encoded OCT-A synthetic images were the least realistic, with malformations in the vasculature as well as in the coloring.

Data extraction

Extraction of the image data from the scanners involved decoding of binary files, anonymization of patient identifiers and association of files to the respective examinations. Anonymous patient identifiers were already created in the context of the two studies where the image data originate from. The eye examinations were stored in the scanners under these IDs. We replaced these identifiers with new pseudo-anonymous keys for the family, patient and eye such that our dataset cannot be directly related to information stored in the scanners. Fundus SLO was extracted as DICOM files and directly anonymized. Image quality was reviewed based on movement or optical distortions such as lash or eyelid coverage and a straight eye gaze was required. Two examples of excluded FAF scans are shown in Figure S2. Initially we intended to use widefield photos which allowed for a more complete depiction of the fundus, but this dataset contained only a small set of images with 74 autofluorescence and 76 red-green images. OCT-A images from the Zeiss Angioplex were evaluated by focus and resolution. Images were exported as .bmp and converted to jpg while sensitive metadata such as study date were removed from the filename. Exported files from the Heidelberg OCT lacked any reference to the examination it contained. Furthermore, these files were encoded as .E2E binary files, for which the scanner manufacturer provides no software to read the data. Therefore we had to decode the files ourselves. By adapting code from <https://github.com/marksgraham/OCT-Converter> to the structure of our data files we managed to extract binary image data, convert it into .npy files and extract patient identifiers with image metadata that allowed for identification of the recording type and follow-up order of examinations as multiple visits per patients were recorded.

Preprocessing

After building the database, images were preprocessed to be used in the neural networks. Preprocessing was the same for the generative models, the filter and the classification models. Pixel values were normalized according to the untrained or pretrained neural networks (ResNet, EfficientNet). In case grayscale images were used on networks designed for RGB, grayscale channels were duplicated to create three-channel tensors. Age inputs were rescaled by 0.01 and sex was encoded as binary 0 (Male) 1 (Female). Fundus SLO images (originally 4000×4000 pixels) were cropped to remove the black background as visible in Figure S2 and then zoomed in to bring the fundus in the field of view and remove the eye lashes. Background and irrelevant structures of the sclera in B-scan OCT images (originally 1536×1536 pixels) were removed by cropping the top and bottom regions with pixel intensity lower than a manually set threshold. All 2-dimensional images were resized to 256×256 pixels. 3D OCT images were resized to $32 \times 128 \times 128$ (raw images: $73 \times 384 \times 496$ (OCT-VONH); $49 \times 512 \times 496$ (OCT-VMAC))

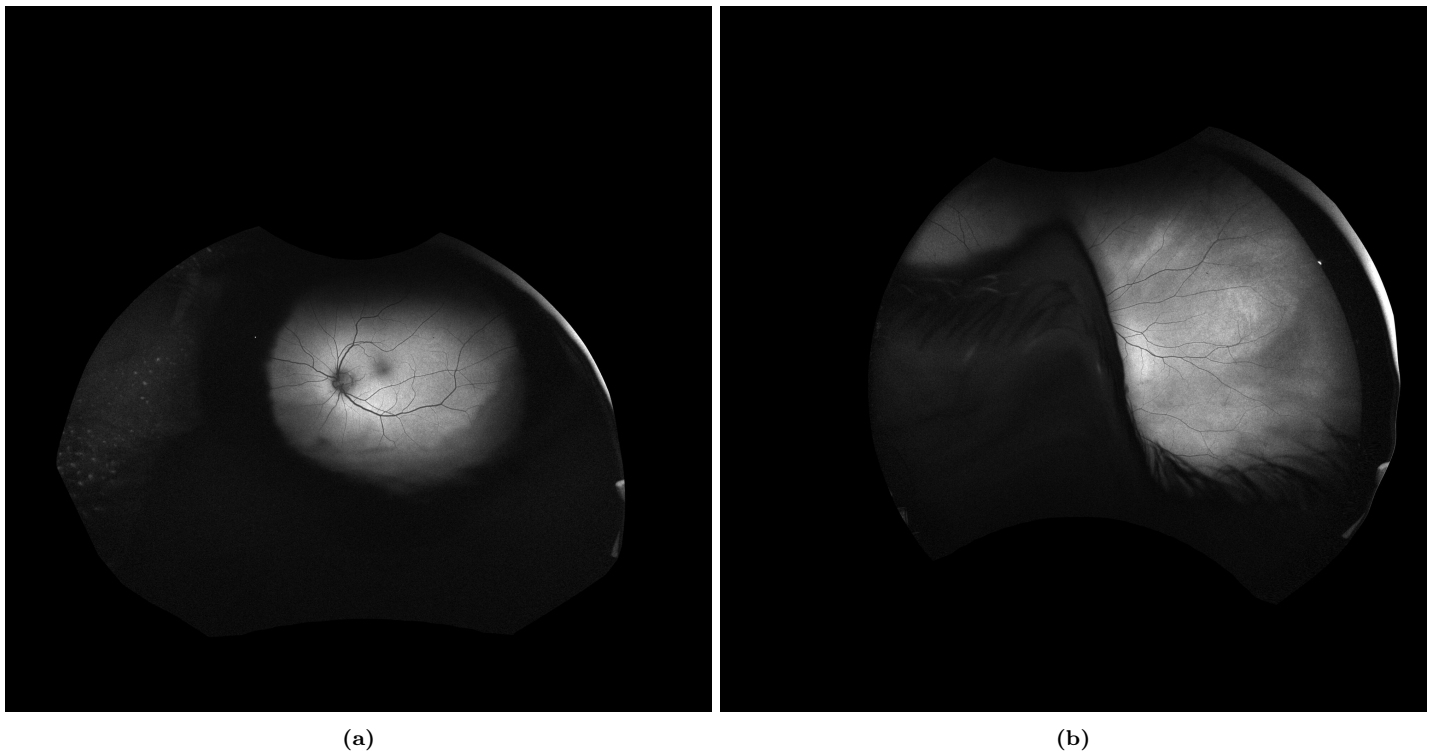


Figure S2: Example of excluded fundus. The two most often occurring reasons for exclusion were insufficient focus (a) and coverage of the fundus by the eyelid or eye lashes (b).

Augmentation

For augmenting the 2D images, random affine (shear, rotate) transformations, color (brightness, contrast), crop and zoom were applied. The zoom factor for B-Scan OCT was left unchanged as interpolation methods resulted in poor image quality. Volumetric 3D OCT was augmented by randomly cropping 75 – 10% of the original volume in the X-Y plane.

Neural networks

The best learning rate, learning rate scheduler and optimizer hyperparameters were obtained through hyperparameter optimization. Model designs and approaches were also selected by comparison of small (25-trial) hyperparameter optimization experiments. Hyperparameter optimization used the Tree-structured Parzen Estimator algorithm through the Optuna Framework. Furthermore, training batches were formed with weighted random sampling to address class imbalance of AmyloidPET labels by oversampling the AmyloidPET+ samples.

All classification models were trained with early stopping: the training process was terminated when evaluation on the validation set showed no improvement. All AmyloidPET classifiers were trained with Focal Loss to emphasize on hard, misclassified examples.[6] The models were trained to output the probability for AmyloidPET- status.

As the model was trained for outputting the probability for AmyloidPET-, these metrics were calculated with inverse ground truth labels and predictions. We calculate the predictions for AmyloidPET+ as $1 - outputs$ and the groundtruth labels for AmyloidPET as $1 - groundtruth$, this way the sensitivity and specificity reflected the model’s performance with respect to detecting AmyloidPET+ cases.

The classification models were evaluated with metrics derived from receiver-operator (ROC) and precision-recall (PR) curves. Precision and recall were determined based on a threshold obtained with the youden’s index.

DDPM

GANs consist of two competing models, a generator produces fake images and a discriminator distinguishes between real and fake images. In this process the generator is secluded from the real images, so there is little risk of the generator producing copies of real images. Unlike GANs, which prioritize image fidelity over diversity and seclude the training images from the generator, DDPMs are prone to memorization as generator has access to information of the training images. This is because the loss is computed between the predicted noise and noise to be removed in the real image. DDPMs initially map an input image to a noise image by gradually adding Gaussian noise in many small steps. Subsequently, the reverse process is learned in small steps by predicting what noise should be removed from a given image at a certain step in the denoising process. A popular implementation of DDPMs involves a U-net-shaped CNN for predicting the noise to be removed. The selected model to produce images corresponding to specific AmyloidPET status was a conditional U-Net DDPM. This model performs conditioning on the timestep embedding that is used for predicting the noise that is to be removed. This conditioning is achieved through addition of the class label embedding vector to the time step embedding vector.

Different configurations for attention levels, filter channels, residual connections and architecture variations such as latent diffusion networks and ControlNets were tested. A conditional DDPM with U-Net backbone was used from the MONAI Generative open-source project.[7] The model was trained to take inputs of 256×256 pixels with three blocks in the encoders and decoders (64, 128 and 128 channels), two residual blocks per encoder/decoder block and spatial transformer attention mechanisms with 32 channels per head in the last encoder/decoder block. The spatial transformer learns to model complex spatial transformations to align the feature maps more accurately with the target distribution. The diffusion model was trained to produce images corresponding to the desired AmyloidPET status by conditioning the U-Net and thereby conditioning the denoising process during training and sampling. This conditioning was achieved through incorporation of the class label embedding into the timestep embedding. The timestep embedding is incorporated into the output by passing it through a linear layer and subsequent summation with the intermediate representation of the input at each block of the UNet. We used a scaled linear beta noise schedule function to add noise to the training images, initial learning rate of $1e^{-3}$, cosine annealing learning rate scheduler, and Adam optimizer without weight decay.

Filter

The network for the filter was an EfficientNetB0 model pretrained on ImageNet. All layers in the model were finetuned during training. The network was trained for 100 epochs with learning rate $1e^{-5}$, Adam optimizer with weight decay of 0.1 and no learning rate scheduler. The training objective was to correctly recognize the modality of an image out of 26 different classes. The model performed well, with Matthew’s Correlation Coefficient (MCC) of 0.9900 for the predictions on the validation set and MCC of 0.9968 on the test set. Results for all modalities are shown in Table S1 and Figure S3. We

tried applying a filter with lower validation accuracy, by training for fewer epochs, in the hope that an image would have to represent its modality very strongly and therefore unrealistic images would be discarded more often. However, this did not make any difference.

Modality (abbreviation)	Modality (explanation)	precision	recall	f1-score
COL	Fundus SLO red-green	1.00	1.00	1.00
FAF	Fundus SLO autofluorescence	1.00	1.00	1.00
OCTA-EMAC	OCT-A Macula Angiography Depth Encoded	1.00	1.00	1.00
OCTA-EONH	OCT-A ONH Angiography Depth Encoded	1.00	1.00	1.00
OCTA-WONH	OCT-A ONH Angiography WholeEye	0.99	1.00	0.99
OCTA-WMAC	OCT-A Macula Angiography WholeEye	1.00	1.00	1.00
OCTA-ORCCMAC	OCT-A Macula Angiography ORCC	1.00	1.00	1.00
OCTA-ORCCONH	OCT-A ONH Angiography ORCC	1.00	1.00	1.00
OCTA-RMAC	OCT-A Macula Angiography Retina	0.95	1.00	0.98
OCTA-RONH	OCT-A ONH Angiography Retina	1.00	1.00	1.00
OCTA-DMAC	OCT-A Macula Angiography Deep	1.00	0.99	0.99
OCTA-DONH	OCT-A ONH Angiography Deep	1.00	1.00	1.00
OCTA-SMAC	OCT-A Macula Angiography Superficial	1.00	0.96	0.98
OCTA-SONH	OCT-A ONH Angiography Superficial	1.00	1.00	1.00
OCT-WONH	OCT ONH Structure WholeEye	1.00	1.00	1.00
OCT-WMAC	OCT Macula Structure WholeEye	1.00	1.00	1.00
OCT-ORCCMAC	OCT Macula Structure ORCC	1.00	1.00	1.00
OCT-ORCCONH	OCT ONH Structure ORCC	1.00	1.00	1.00
OCT-RMAC	OCT Macula Structure Retina	0.99	1.00	0.99
OCT-RONH	OCT ONH Structure Retina	1.00	1.00	1.00
OCT-DMAC	OCT Macula Structure Deep	1.00	0.97	0.99
OCT-DONH	OCT ONH Structure Deep	1.00	1.00	1.00
OCT-SMAC	OCT Macula Structure Superficial	1.00	1.00	1.00
OCT-SONH	OCT ONH Structure Superficial	1.00	1.00	1.00
OCT-BMAC	OCT Macula B-Scan	1.00	1.00	1.00
OCT-BONH	OCT ONH B-Scan	1.00	1.00	1.00
weighted avg		1.00	1.00	1.00

Table S1: Accuracy of filter

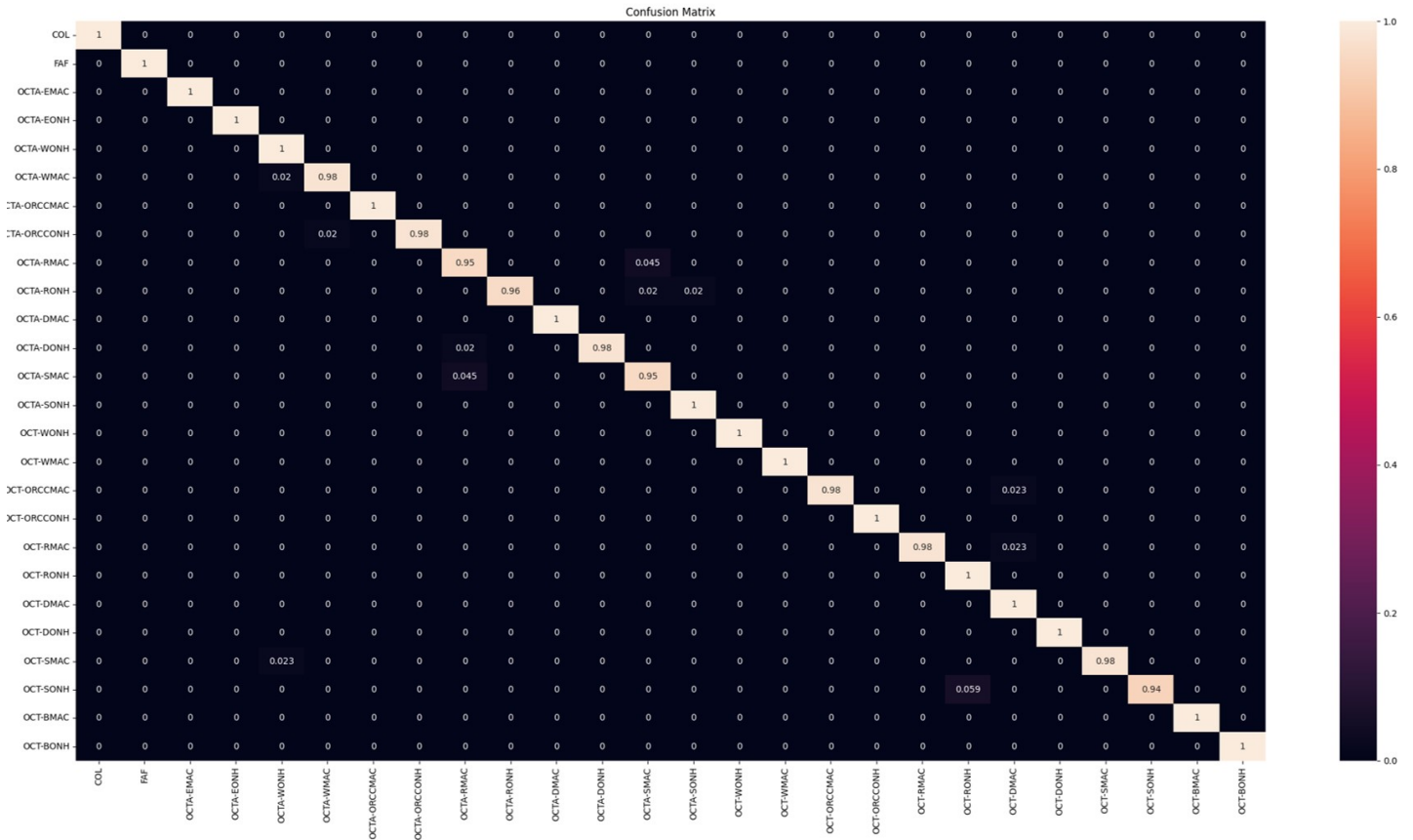


Figure S3: Confusion matrix for distinguishing between 26 modalities by the filter. Wrong predictions happened among modalities that were relatively similar.

Unimodal classifiers

ResNet and the EfficientNet family architectures were explored in combination with and without pre-trained ImageNet weights as starting points. In addition to modality-specific classifiers we also experimented with training one shared modality-aware classifier with feature-wise linear modulation (FiLM) but this did not perform well.[8]

The starting point for the unimodal classifiers was a EfficientNetB0 network without pretrained weights. The final layer was changed to a binary prediction layer. Classifiers were trained for 200 epochs with various initial learning rates, a step LR scheduler and Adam optimizer without weight decay. Binary cross entropy was compared with Focal Loss in 20-trial hyperparameter experiments. As the loss stopped converging throughout the 200 epochs we selected model checkpoints taken from the best epoch.

Multimodal classifiers

The multimodal classifier is a fusion of the unimodal classifiers through fully connected layers for combining unimodal predictions and metadata. We experimented with various fusion methods, none of these fusion methods outperformed our selected approach (i.e. heterogeneous fusion). The methods we experimented with were:

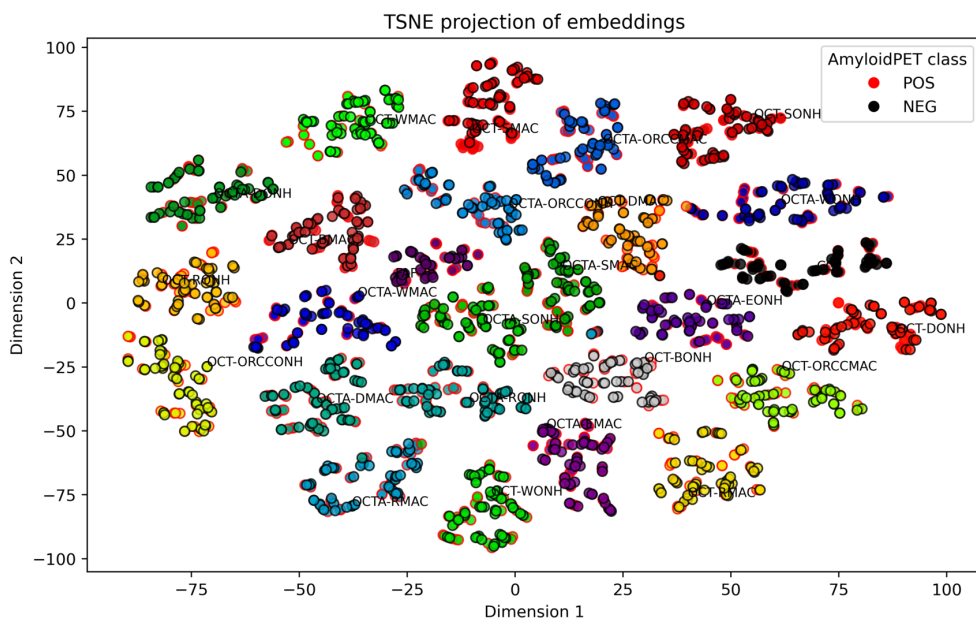
- Fusion of embedding vectors produced by the unimodal classifiers by transforming the vectors into 2-dimensional arrays and applying convolution operations on the resulting multi-channel vectors and several fully connected layers at the end.
- Fusion of embedding vectors produced by the unimodal classifiers through multiple fully connected layers.
- Early or late fusion of metadata with classification features through either incorporation of metadata early in the fully connected network or late in the fully connected network.

As the loss on the validation set stopped converging but would not deteriorate throughout the 200 epochs, we would select the model checkpoint from the last epoch.

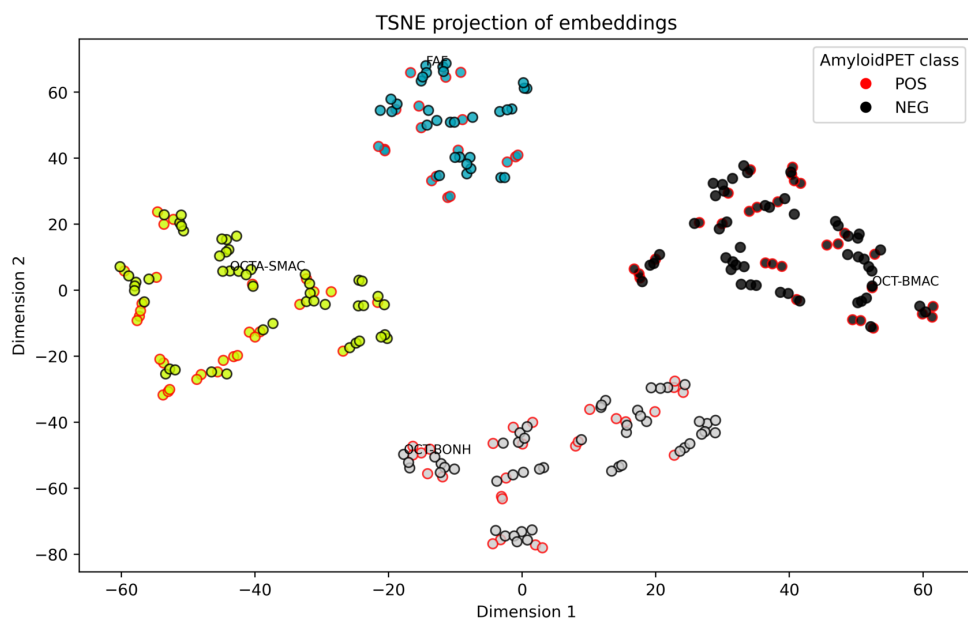
Modality-aware classifier with FiLM

As the filter model successfully distinguished modalities, we experimented with training one modality-aware classification network that was capable of predicting AmyloidPET status for any of the four modalities through an additional input that informed the model of the modality type. This additional input was an embedding vector extracted from the first fully connected layer of the filter model. Figure S4 displays these embeddings on reduced 2-dimensional axes for all images in the test set and demonstrates that this embedding was suitable for distinguishing modality types. Although FiLM-based classification performed poorly, we show the filter embeddings in Figure S4 to demonstrate that AmyloidPET status was not correlated in the embedding space and therefore the filter was not biased towards a specific AmyloidPET group.

The embeddings were used in the modality-aware classifier by conditioning intermediate activations of the classification networks in FiLM layers. Through FiLM, the intermediate outputs of selected layers of a neural network are transformed with scale and bias parameters. These parameters are mapped from a given conditioning embedding, in our case the filter embedding. The mapping from embedding vector to a scale and bias parameter is learned during model training, as part of the same back-propagation chain as the rest of the model training. As a result, the scale and bias parameters learn to modulate the model operations according to the embedding vector that describes the image modality. We added two FiLM layers in each network: one between the stem and Block 1 and between Block 2 and Block 3.



(a)



(b)

Figure S4: TSNE projection of filter embedding of (a) images of all modalities and (b) the modalities used in the classification experiments. Modalities can be distinguished by filling color. AmyloidPET status is distinguished by edge color, with which we want to demonstrate that the embedding space is not correlated to AmyloidPET status. TSNE embeds the points from a higher dimension to a lower dimension trying to preserve the neighborhood of that point by minimizing the Kullback–Leibler divergence between distributions with respect to the locations of the points in the map. Projections (a) and (b) come from TSNE calculations with different sets of modalities which results in different projections of the OCT-SMAC, OCT-BONH, OCT-BMAC and FAF points on the 2D spaces.

Class activation maps

We implemented Gradient-weighted CAM (GradCAM) with the library `pytorch-grad-cam` to produce heatmaps that give insight into the model’s activations after the last convolutional layer.[9] Since the activity of convolutional layers often maps spatially to the input, we upsampled the GradCAM attributions to mask the input. GradCAM applied to our binary classification network computed the gradient of the binary output layer with respect to each of the network’s activations at the

selected convolutional layer. To produce the heatmap, the gradient at the output layer was computed and subsequently multiplied with the layer’s activations. We depict GradCAMs as a heatmap in which the red-orange color regions were the most discriminative areas for the model to predict AmyloidPET- and the green-blue areas were the least salient. Figures S5-S7 contain the same retinal images, allowing for direct comparison of the heatmaps of different classifiers.

The GradCAM heatmaps for the three different classifiers trained on OCTA-SMAC showed different patterns. The classifier trained on real images showed highest response to blood vessels in the periphery and there is a larger area of high response to real images than synthetic images. In contrast, the pretrained classifier showed a larger response area in the center of the image. The response to the synthetic images was different, with high responses to a large central area. The model trained on synthetic images displayed attention to small areas in the periphery. We did not observe large differences in the size of the heatmap areas with high response between true negative and true positive images, except for the heatmaps on real images produced by the classifier trained on synthetic images. This was also reflected by the small differences in output values. Attention of the OCT-BMAC classifiers did not show that clinically related features were learned by the model. The baseline FAF classifier attended to the periphery of the fundus.

The OCT-BONH classifier trained on real images showed high response to small areas in the layers of the retina. The pretrained classifier showed responses to similar areas, with slightly larger areas of high activation in the pretrained images. The shape and location of the high response areas implied that these models learned to identify meaningful features, however the output values for the different classes were very close to each other (0.494 and 0.485 compared to 0.471 and 0.489) which implies that the classes were not well distinguished by these features. The classifier trained on synthetic data showed larger areas of high response, even more so in the real images compared to synthetic images. In contrast, the pretrained FAF classifier identified areas around the fovea and ONH.

The pretrained OCT-BMAC classifier showed very little response in any of the images, except for the heatmap on the real AmyloidPET+ images which depicted a localized response in the photoreceptor layer and retinal pigment epithelium. Interestingly, the classifier trained on real images showed localized response to a synthesis artifact in the synthetic AmyloidPET- images. The heatmaps produced by this classifier seemed different for the images, nonetheless the confidence for AmyloidPET- was similar. In contrast, the classifier trained on synthetic images showed a low response to the synthesis artifact. The responses were more localized than in the classifier trained on real images.

The GradCAM heatmaps for the three different classifiers trained on FAF showed different patterns. The pretrained model identified areas around the fovea and ONH. For both synthetic and real images there were slightly larger areas of high response which was also reflected in the output scores. The model trained on synthetic images showed responses of very different shapes when comparing the synthetic and real images. The synthetic images showed a large squared area of high response whereas the response to real images was more restricted to specific areas, mostly in the periphery of the fundus. The model trained on real images showed strongest responses in small areas of the far periphery of the fundus. This model produced larger areas of high response to the synthetic images. These responses were more localized around the ONH and fovea.

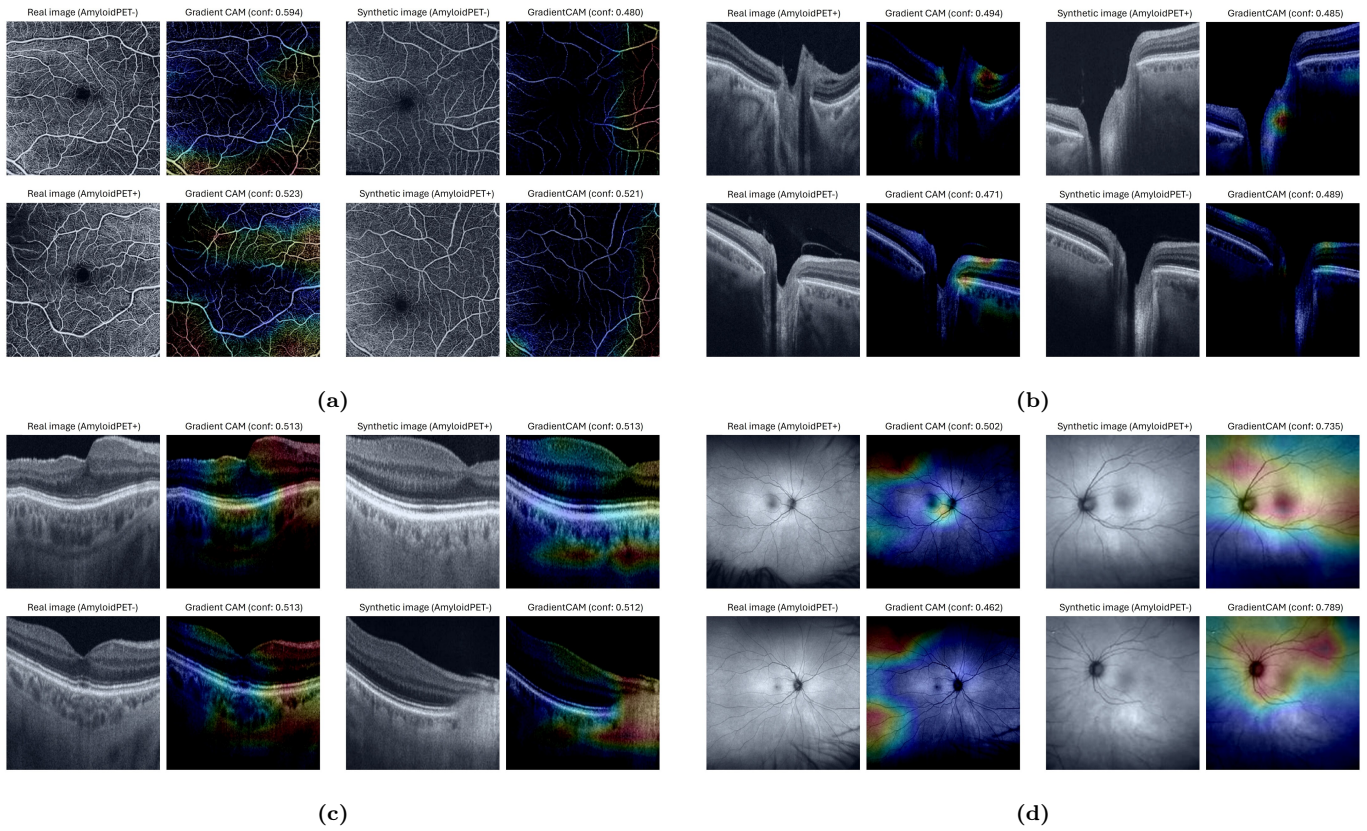


Figure S5: GradCAMs generated for classifiers trained on real images only. The subfigures show pairs of input images and GradCAM heatmaps for OCTA-SMAC (a), OCT-BMONH (b), OCT-BMAC (c), FAF (d). Each subfigure has four images. Left top to bottom: real images for AmyloidPET+ and AmyloidPET-. Right top to bottom: synthetic Images for AmyloidPET+ and AmyloidPET-.

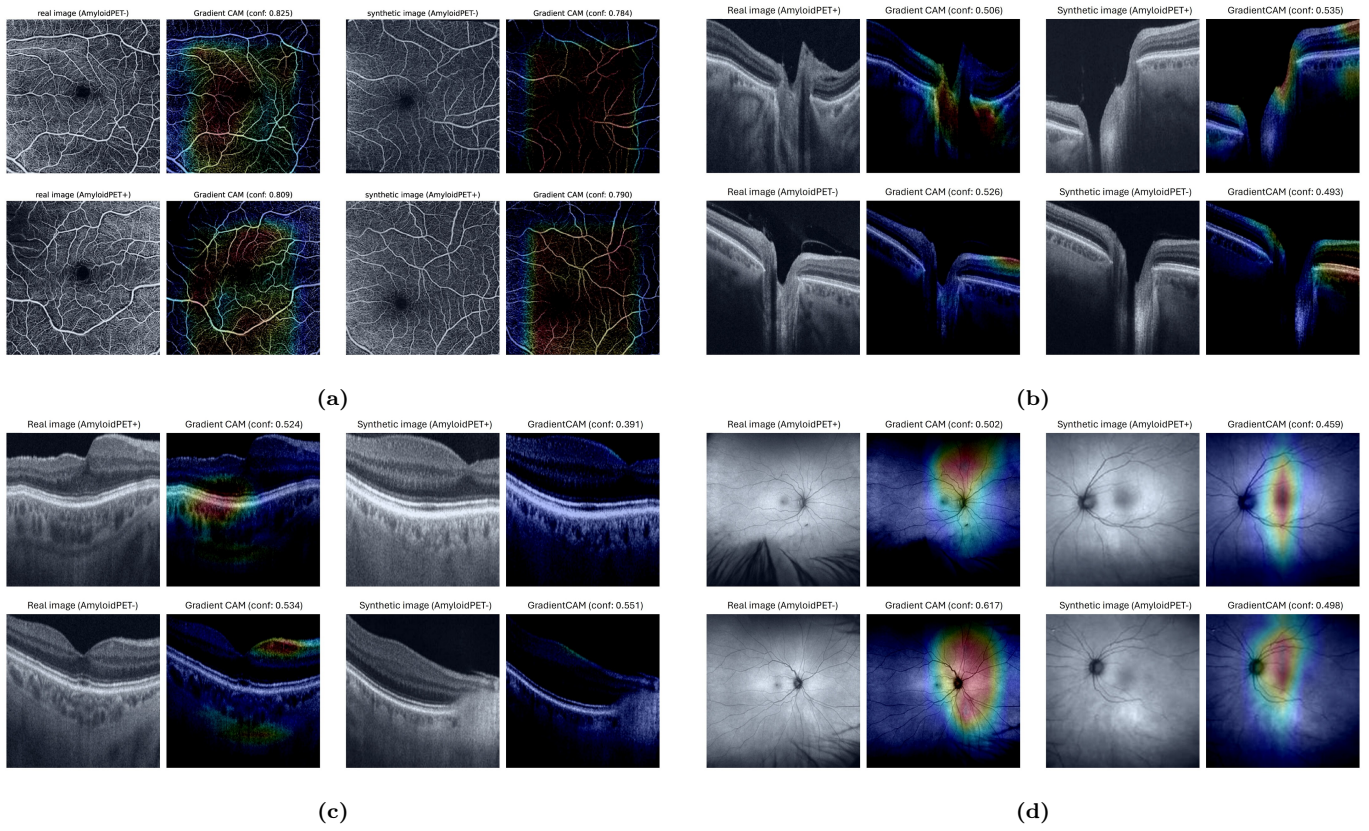


Figure S6: GradCAMs generated for classifiers pretrained on synthetic images and finetuned on real images. The subfigures show pairs of input images and GradCAM heatmaps for OCTA-SMAC (a), OCT-BMONH (b), OCT-BMAC (c), FAF (d). Each subfigure has four images. Left top to bottom: real images for AmyloidPET+ and AmyloidPET-. Right top to bottom: synthetic images for AmyloidPET+ and AmyloidPET-.

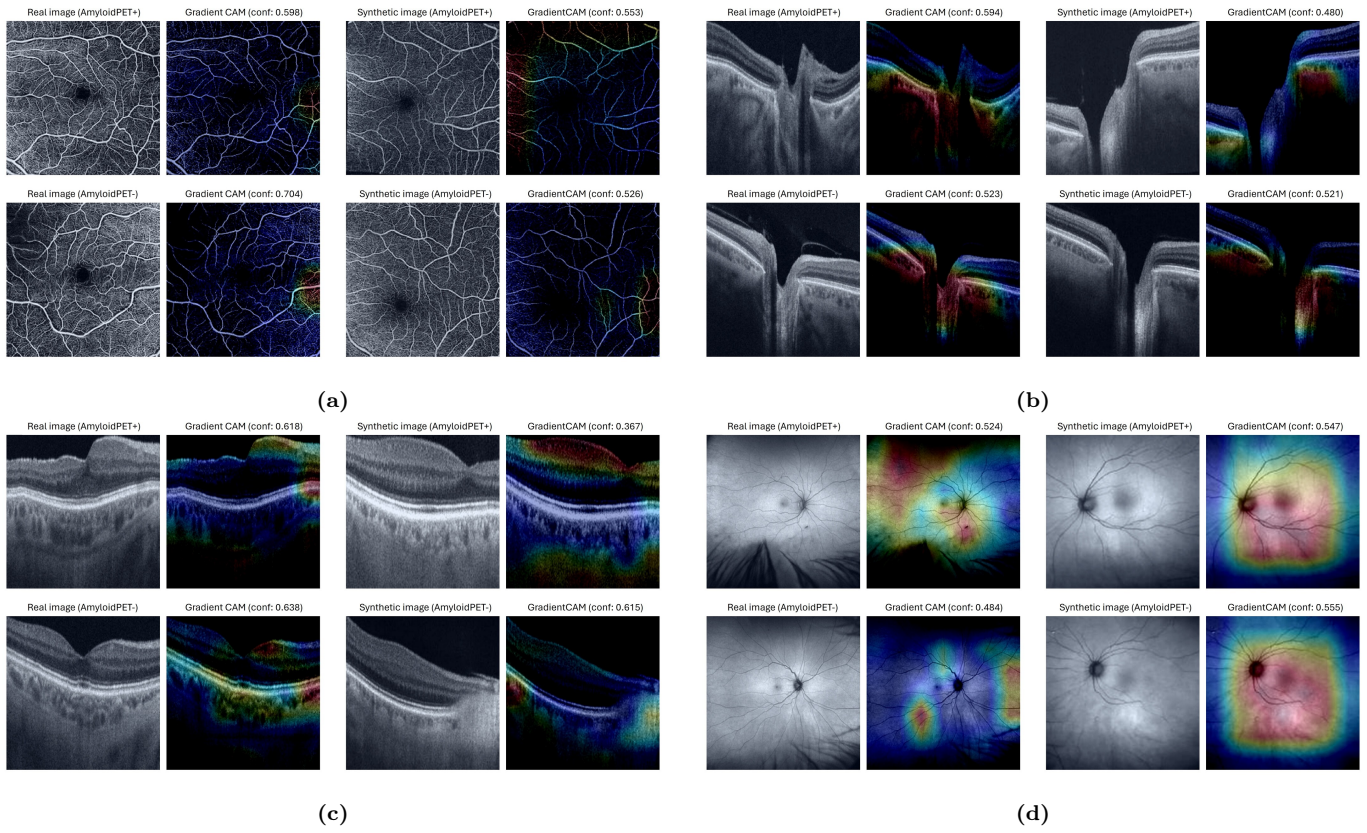


Figure S7: GradCAMs generated for classifiers trained on synthetic images only. The subfigures show pairs of input images and GradCAM heatmaps for OCTA-SMAC (a), OCT-BMONH (b), OCT-BMAC (c), FAF (d). Each subfigure has four images. Left top to bottom: real images for AmyloidPET+ and AmyloidPET-. Right top to bottom: synthetic Images for AmyloidPET+ and AmyloidPET-.

References

1. Konijnenberg E, Carter SF, Kate M ten, Braber A den, Tomassen J, Amadi C, Wesselman L, Nguyen HT, Kreeke JA van de, Yaqub M, Demuru M, Mulder SD, Hillebrand A, Bouwman FH, Teunissen CE, Serné EH, Moll AC, Verbraak FD, Hinz R, Pendleton N, Lammertsma AA, Berckel BNM van, Barkhof F, Boomsma DI, Scheltens P, Herholz K, and Visser PJ. The EMIF-AD PreclinAD study: study design and baseline cohort overview. *Alzheimer's Research & Therapy* 2018 Aug; 10. DOI: 10.1186/s13195-018-0406-7
2. Kreeke JA van de, Nguyen HT, Haan J den, Konijnenberg E, Tomassen J, Braber A den, Kate M ten, Collij L, Yaqub M, Berckel B van, Lammertsma AA, Boomsma DI, Tan HS, Verbraak FD, and Visser PJ. Retinal layer thickness in preclinical Alzheimer's disease. *Acta Ophthalmologica* 2019 May; 97:798–804. DOI: 10.1111/aos.14121
3. Katsimpris A, Karamaounas A, Sideri AM, Katsimpris J, Georgalas I, and Petrou P. Optical coherence tomography angiography in Alzheimer's disease: a systematic review and meta-analysis. *Eye* 2021 Jun; 36:1419–26. DOI: 10.1038/s41433-021-01648-1
4. Jin Q, Lei Y, Wang R, Wu H, Ji K, and Ling L. A Systematic Review and Meta-Analysis of Retinal Microvascular Features in Alzheimer's Disease. *Frontiers in Aging Neuroscience* 2021 Jun; 13. DOI: 10.3389/fnagi.2021.683824
5. Ashraf G, McGuinness M, Khan MA, Obtinalla C, Hadoux X, and Wijngaarden P van. Retinal imaging biomarkers of Alzheimer's disease: A systematic review and meta-analysis of studies using brain amyloid beta status for case definition. *Alzheimer's & Dementia: Diagnosis, Assessment & Disease Monitoring* 2023 Apr; 15. DOI: 10.1002/dad2.12421
6. Lin TY, Goyal P, Girshick R, He K, and Dollár P. Focal Loss for Dense Object Detection. 2017. DOI: 10.48550/ARXIV.1708.02002
7. Pinaya WHL, Graham MS, Kerfoot E, Tudosiu PD, Dafflon J, Fernandez V, Sanchez P, Wolleb J, Costa PF da, Patel A, Chung H, Zhao C, Peng W, Liu Z, Mei X, Lucena O, Ye JC, Tsiftaris SA, Dogra P, Feng A, Modat M, Nachev P, Ourselin S, and Cardoso MJ. Generative AI for Medical Imaging: extending the MONAI Framework. 2023. DOI: 10.48550/ARXIV.2307.15208
8. Perez E, Strub F, Vries H de, Dumoulin V, and Courville A. FiLM: Visual Reasoning with a General Conditioning Layer. 2017. DOI: 10.48550/ARXIV.1709.07871
9. Selvaraju RR, Cogswell M, Das A, Vedantam R, Parikh D, and Batra D. Grad-CAM: Visual Explanations from Deep Networks via Gradient-Based Localization. *International Journal of Computer Vision* 2019 Oct; 128:336–59. DOI: 10.1007/s11263-019-01228-7